中国激光

血管内光声-超声-光学相干层析-光声弹性多模态成像方法及系统

万余洋[1,2]，雷鹏[3*]，熊科迪[1,2]，杨思华[1,2**]

[1]华南师范大学生物光子学研究院，激光生命科学教育部重点实验室暨激光生命科学研究所，广东 广州 510631；
[2]华南师范大学生物光子学研究院，广东省激光生命科学重点实验室，广东 广州 510631；
[3]广东省科学院生物与医学工程研究所，广东 广州 510316

摘要 识别动脉粥样硬化斑块的易损性是防治急性冠状动脉疾病的重要途径。纤维帽厚度、脂质核心大小、管腔狭窄程度和管腔的力学特性是评估斑块易损性的关键参数。然而，单一模态的血管内成像技术难以通过一次成像获取用于评估斑块易损性的全面信息。本团队通过复用光路和声路，将血管内超声成像(IVUS)和血管内光学相干层析成像(IVOCT)与血管内光声成像(IVPA)、光声弹性成像(IVPAE)有机结合到一起，开发了一种血管内光声-超声-光学相干层析-光声弹性四模态一体化成像探头及成像系统。该一体化成像探头的成像直径仅为0.97 mm，光学相干层析、光声、超声模态的横向分辨率分别为20.5、61.3、122.2 μm，纵向分辨率分别为15.8、57.4、72.5 μm。离体模拟样品和兔腹主动脉的在体成像实验验证了血管内四模态成像能够提供血管壁的宏观和微观结构信息，同时能够特异性识别脂质成分和反映脂质斑块的弹性力学信息。该一体化探头可一次性获取血管内斑块的多物理影像特性，有望为动脉粥样硬化斑块的深入理解和诊治提供新型的介入成像方法和工具。

关键词 医用光学；光声成像；超声成像；光学相干层析成像；光声弹性成像；血管内多模态成像

中图分类号 Q631 **文献标志码** A **DOI**：10.3788/CJL221028

1 引 言

动脉粥样硬化斑块破裂并伴有血栓形成是大多数急性冠状动脉综合征和猝死的公认原因。其中，斑块的结构和组成是评估斑块易损性的决定因素[1-3]。易损斑块被定义为破裂风险升高的非阻塞性病变，其典型特征包括薄的纤维帽、富含脂质的坏死核心和严重狭窄[4-6]。此外，斑块的脆弱性还会受到血管壁和斑块力学特性的影响[7-8]。在临床上，利用介入手术获取血管内斑块的结构和组成信息对于诊断和选择适当的治疗策略具有重要作用。

目前，一些血管内成像技术已被成功应用于斑块信息的检测和表征[9-11]，其中，血管内超声(IVUS)和血管内光学相干断层扫描(IVOCT)是临床上血管内成像常用的技术手段。IVUS具有较大的穿透深度，可用于测量管腔面积、斑块负荷和血管形态重塑[12]；然而，IVUS的轴向分辨率有限，不能精确测量纤维薄帽。IVOCT具有微米级别的分辨率，能够评估薄纤维帽的准确厚度[13-15]；然而，IVOCT信号的穿透力较小，成像深度有限，无法确定坏死核心的大小。同时，上述两种手段均难以对斑块的力学特性进行测量。血管内光声成像(IVPA)是一种新兴的血管内成像技术，可以在高达几厘米的穿透深度下提供亚毫米级别的分辨率，并且能够通过特定的吸收波长以高灵敏度和特异性定位、成像脂质[16-19]。本研究团队前期提出了血管内光声弹性成像(IVPAE)方法，该方法能够通过IVPA技术在无额外激励的情况下对斑块进行弹性成像[19-20]，进而评价血管内斑块的弹性力学性质。然而，目前还没有一种单一的血管内成像方法能够对动脉粥样斑块的易损性进行全面诊断。斑块的易损性与斑块的结构、组分和力学特性高度相关[7,21]。临床医生需要获取多种特征才能对斑块进行全面识别和评估[22]。近年来，国内外已经报道了用于血管内斑块多参数评估的数种多模态血管内成像系统，如IVUS-IVPA[23-30]、IVPA-IVOCT[31]、IVUS-IVOCT[32]、IVUS-IVPA-IVOCT[33-34]、IVPA-IVUS-IVPAE[20]等。可见，血管内

收稿日期：2022-07-05；**修回日期**：2022-07-28；**录用日期**：2022-08-05；**网络首发日期**：2022-09-27

基金项目：国家自然科学基金(61822505，61627827)、广东省自然科学基金(2022A1515010548，2022A1515011247)、广东省科学院建设国内一流研究机构行动专项资金项目(2021GDASYL-20210103031)、广州市科技计划项目(2019050001)

通信作者：*leipeng@scnu.edu.cn；**yangsh@scnu.edu.cn

多模态成像技术已经成为研究热点，而一次成像就可以获取斑块的多种模态信息已成为重要的发展趋势。

本研究团队提出并研发了一种血管内多模态一体化成像探头及系统。该系统将IVPA、IVUS、IVOCT和IVPAE四种成像模态集于一体，通过单个微型探头（直径为0.97 mm）进行360°旋转和同步回撤进行一次成像即可获取血管内斑块四种不同模态的影像学信息。

2　实验装置

2.1　多模态系统的成像原理与一体化探头设计

血管内光声-超声-光学相干层析-光声弹性（PA-US-OCT-PAE）成像系统的原理如图1（a）所示，该多模态系统由4个子系统构成。在光声成像子系统中，可调谐脉冲激光器（NT200）输出波长为1720 nm、重复频率为2.5 kHz的脉冲激光，其作为光声信号的激发光，先经过两个透镜整形，之后由单模光纤耦合器

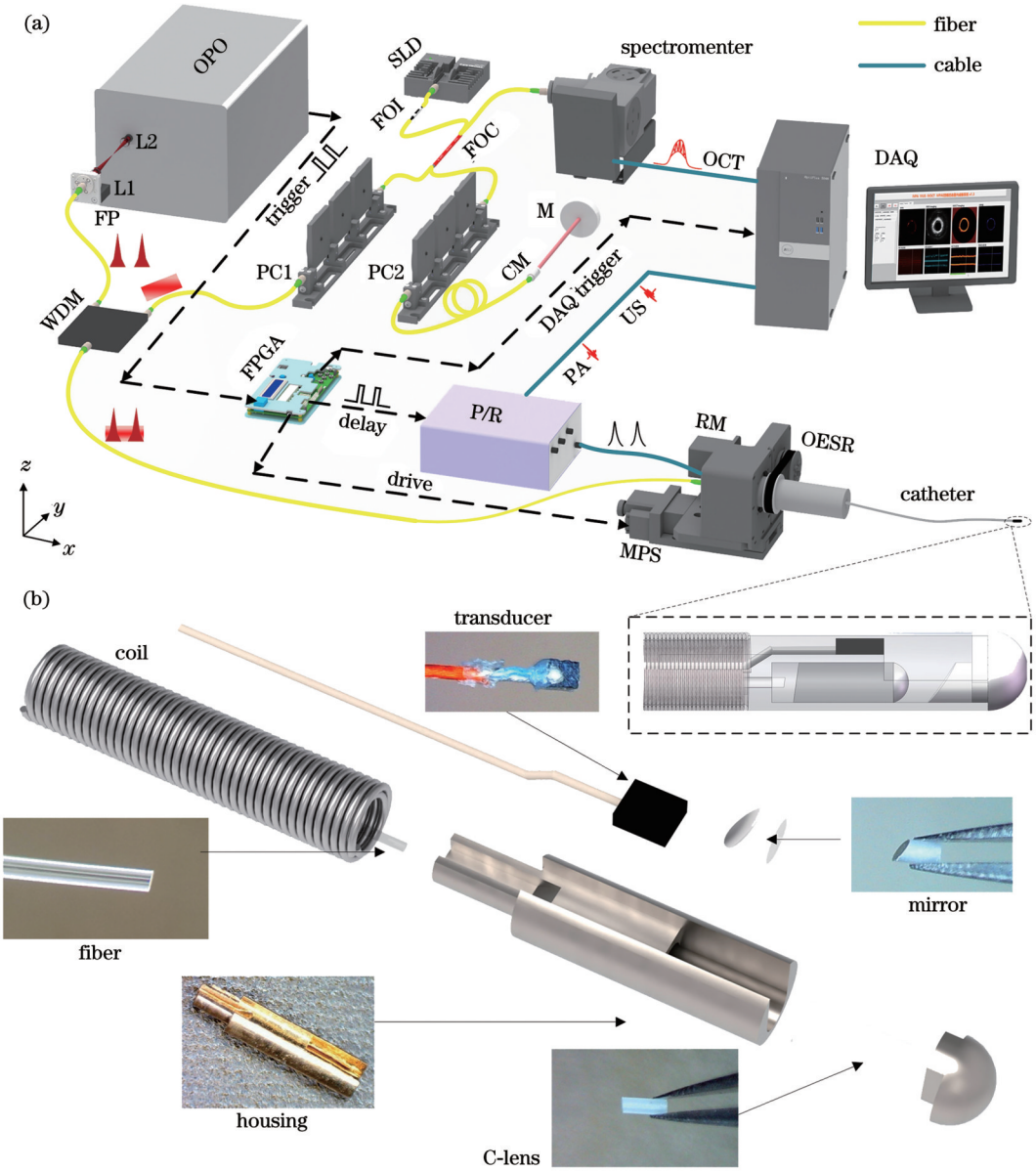

OPO: optical parametric oscillator; L1–L2: lens; FP: fiber port; WDM: wavelength division multiplexer; FOI: fiber optical isolator; SLD: super luminescent diode; FOC: fiber optical coupler; PC1–PC2: polarization controller; CM: collimator; M: mirror; FPGA: field programmable gate array; P/R: ultrasound pulser/receiver; PA: photoacoustic signal; US: ultrasound signal; OCT: optical coherence tomography signal; DAQ: data acquisition system; OESR: optical and electric slip ring; MPS: motorized pull-back stage; RM: rotary motor

图1　血管内光声-超声-光学相干层析光声弹性成像系统原理图以及一体化探头设计组装示意图。（a）四模态成像系统原理图；（b）一体化成像探头设计组装方案示意图以及各部件实物图

Fig. 1　Schematics of intravascular PA-US-OCT-PAE imaging system and design and assemblage of integrated probe. (a) Schematic of four-modality imaging system; (b) design and assemblage scheme of integrated imaging probe and photographs of each component

(PAF2P-A15C)耦合到单模光纤(smf-28e)中,再经由波分复用器(定制)、光电滑环(定制)传输到探头并出射到血管内壁。血管内壁的脂质成分受激之后产生光声信号,光声信号由超声换能器(定制,主频30 MHz,中国科学院苏州生物医学工程技术研究所)接收,接着经光电滑环传输和放大之后被数据采集卡(M-3i.4120)采集,最后经过软件处理后重建得到光声图像。在超声子系统中,OPO激光器输出的同步脉冲信号作为时钟触发输入到现场可编程门阵列(FPGA),FPGA产生一个5 μs的延迟触发信号并传输到超声收发仪(5073P/R型);超声收发仪收到触发信号之后产生超声激励,超声激励通过光电滑环传输到一体化探头的超声换能器中发射超声信号,回波超声信号经过与光声信号相同的路径放大之后由数据采集卡数字化到计算机中,然后采用软件进行数据处理就可以显示超声图像。OCT子系统采用的是光谱域OCT(SD-OCT)系统的基本设计。超连续激光二极管(SLD1325)发出的中心波长为1325 nm、带宽大于100 nm的激光作为光学相干层析检测光,其经过光隔离器(IO-H-1310APC)之后输入到10∶90的2×2耦合器(TW1300-R2A2)的一端,其中:10%的检测光经过偏振控制器(FPC562)后到达参考臂光路,参考臂光路由准直透镜(F260APC780)和反射镜(PF20-03-M01)组成;90%的检测光经过偏振控制器(FPC562)后经过波分复用器和光电滑环,之后由一体化成像探头出射到达血管内壁,并被反射回去。样品臂的回光和参考臂的回光在耦合器中发生干涉,并传输到自研的光谱仪中。干涉光被光谱仪中的光栅分光后被线阵CCD(GL2048L)采集,并由帧接收器(PCIe-1433)数字化到计算机中。最终,光谱信号经过软件处理之后便可得到光学相干层析图像。在光声弹性子系统中,先用软件对光声信号进行处理,提取光声信号的上升沿时间,再次进行处理后得到光声弹性图像。上述4个模态的成像系统均由LabVIEW软件控制,最终的四模态图像同时显示在成像界面上。

内窥探头对于成像系统来说是至关重要的部分。目前,血管内成像探头在尺寸、频率和功能上都在不断发展。目前报道的血管内光学相干层析成像探头的尺寸包括外套管在内仅为0.457 mm[35],血管内光声成像探头直径最小仅为0.7 mm[27],但其为非聚焦的光声成像探头。此外,多主频的超声换能器以及新兴的超声换能器(如电容式微超声换能器、压电微机械超声换能器)也被用于内窥成像[36-38]。

本团队设计了直径仅为0.97 mm的四模态一体化成像探头,该一体化成像探头的设计结构如图1(b)所示,采用双层并行结构,即光路和声路平行放置。在声路上,主频为30 MHz的微型超声换能器用于光声信号接收、超声信号激发和超声回波信号接收。在光路上,一根具有8°角端面的单模光纤(定制,深圳福津光电技术有限公司)用于传输光声激发光、光学相干层析检测光以及接收光学相干层析的背向散射光;直径为0.5 mm的C-Lens(定制,福州市共信光电技术有限公司)用于光束的聚焦,并通过镀膜反射镜(定制,深圳铭创光电科技有限公司)对光束进行偏折,使光焦点位于超声换能器正上方约2 mm位置处。光路和声路均由探头外壳(定制,深圳市拓维模型技术有限公司)进行固定;探头外壳与扭力线圈(定制,Asahi Intecc,日本)连接,用于力矩传导,使探头进行360°旋转。装配完成后的一体化成像探头的三维示意图如图1(b)右上角所示。经过反复测试,采用该方案装配的探头能够获取稳定的信号,并且,采用该方案组装的成像探头仅有3.6 mm的刚性长度,提升了探头在迂曲血管中的可通过性。

2.2 多模态成像系统电路与控制

为了使血管内光声-超声-光学相干层析-光声弹性多模态成像系统有序进行光/声激发、信号采集和图像重建,本团队设计了相应的电路控制和信号激发采集系统,如图2所示。图2(a)为四模态系统中关键元件的电气连接框图。该系统将OPO激光器的同步触发信号作为系统运行的逻辑起点,利用FPGA内部的逻辑单元对系统时序进行同步,并进行5路输出。其中:Output 1不进行任何延时便触发光声采集卡采集光声超声信号;Output 2延时5 μs进行超声信号的触发,光声信号和超声回波信号经过5 MHz高通滤波和39 dB放大后连接至采集卡;Output 3延时10 μs触发帧接收器采集线阵CCD接收到的干涉光谱信号;Output 4延时15 μs触发步进电机带动探头末端旋转0.72°;Output 5延时200 ms(探头旋转360°)触发步进电机带动探头回撤0.1 mm。系统工作时序图如图2(b)所示,该时序能够保证成像系统进行稳定的分时间隔高速扫描和采集。

2.3 集成成像系统

根据系统原理图和电路时序控制原理,本团队对四模态成像系统进行集成搭建,搭建得到的血管内多模态成像系统实物如图3(a)所示。该系统由SD-OCT系统、OPO激光器、光电处理单元、探头连接单元和成像探头5个子模块组成。SD-OCT系统包含光源、隔离器、耦合器、偏振控制器、光谱仪以及参考臂6个部分,并按照图1(a)所示光学相干层析成像模块的设计原理进行集成。其中,样品臂光纤与光电处理单元通过波分复用器进行连接。OPO激光器输出的波长为1720 nm、重复频率为2.5 kHz的光声激发光通过单模光纤耦合器耦合到单模光纤中,然后输入光电处理单元。光电处理单元包括由FPGA开发板、超声收发仪、电机驱动器、电源组成的电处理单元以及由1720 nm和1310 nm波分复用器构成的光处理单元。

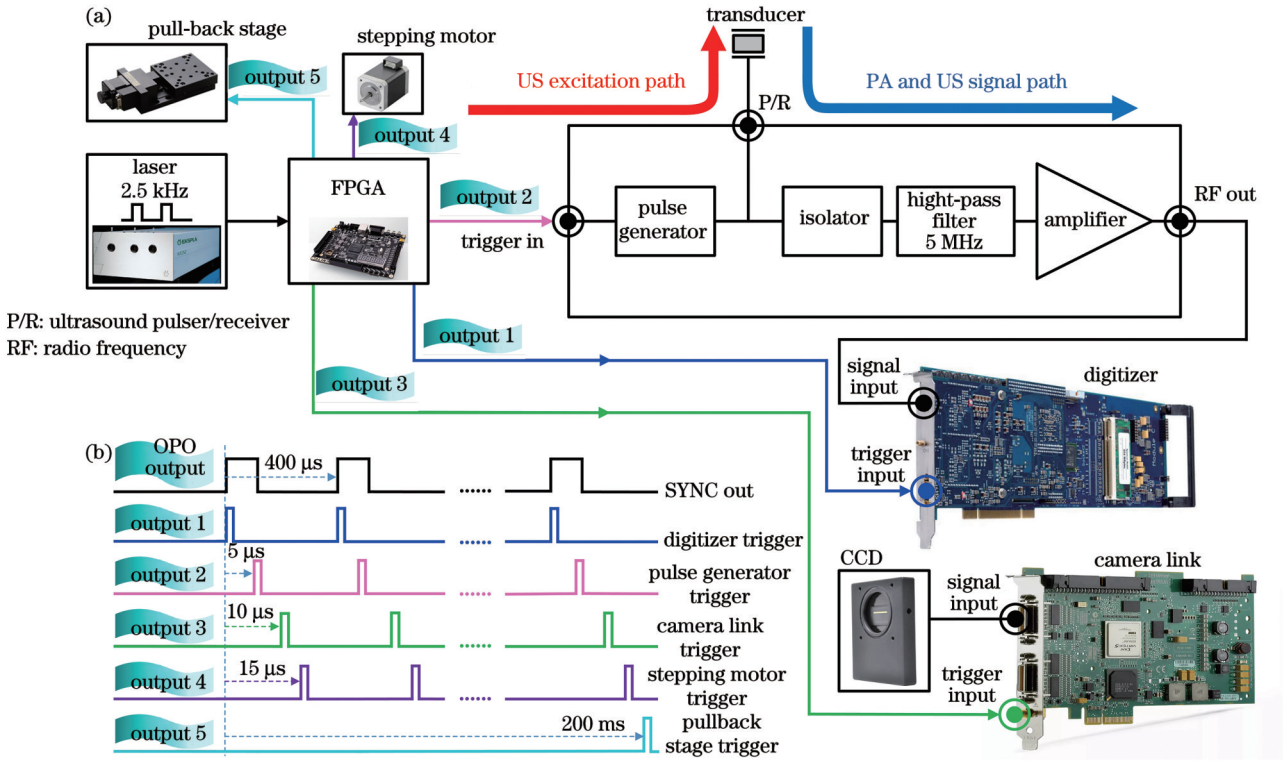

图 2　血管内四模态成像系统的电路逻辑及时序控制。(a)关键元件的电气连接框图;(b)系统控制时序图

Fig. 2　Circuit logic and sequence control of intravascular four-modality imaging system. (a) Block diagram depicting electric connection of key elements; (b) diagram of system timing control

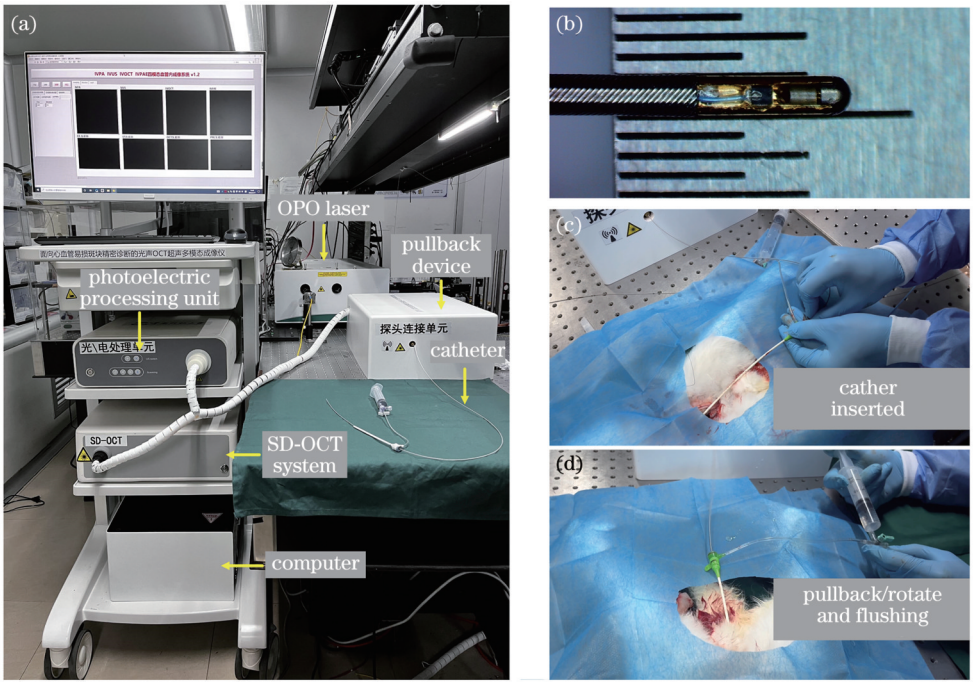

图 3　血管内四模态成像系统及一体化探头的实物图以及活体兔子介入实验照片。(a)组装完成的四模态系统实物照片;(b)一体化成像探头实物图;(c)～(d)兔子在体介入成像操作实验

Fig. 3　Photographs of intravascular four-modality imaging system and integrated imaging probe, as well as *in vivo* experimental demonstration of intervention in rabbit model. (a) Photograph of assembled intravascular four-modality imaging system; (b) photograph of integrated imaging probe; (c)–(d) *in vivo* interventional imaging operation experiment of rabbit

光电处理单元通过电缆(电机驱动信号)、同轴线缆(光声、超声信号)、单模光纤(合束的光声激发光和光学相干层析检测光)与探头连接单元进行连接。探头连接单元由图 1(a)所示的旋转回撤装置封装而成,并通过同轴线缆、光电滑环与成像探头进行连接。成像探头中的光声激发光和光学相干层析检测光最终

从探头末端光路出射，光声信号、超声激发信号和超声回波信号由探头末端的超声换能器进行接收和激发。直径为 0.97 mm 的一体化探头末端的实物图如图 3(b)所示。进一步，本团队利用该四模态成像装置进行离体实验和活体兔子实验，图 3(c)、(d)展示了进行兔腹主动脉在体成像实验时的探头置入和冲刷过程。

3　实验结果

3.1　系统性能测试

搭建完成四模态成像系统后，对该系统的相关性能参数进行测试。首先，为了测试系统超声换能器的探测主频，将探头末端对准钢尺进行超声回波测试，得到的超声回波信号如图 4(a)所示。通过对

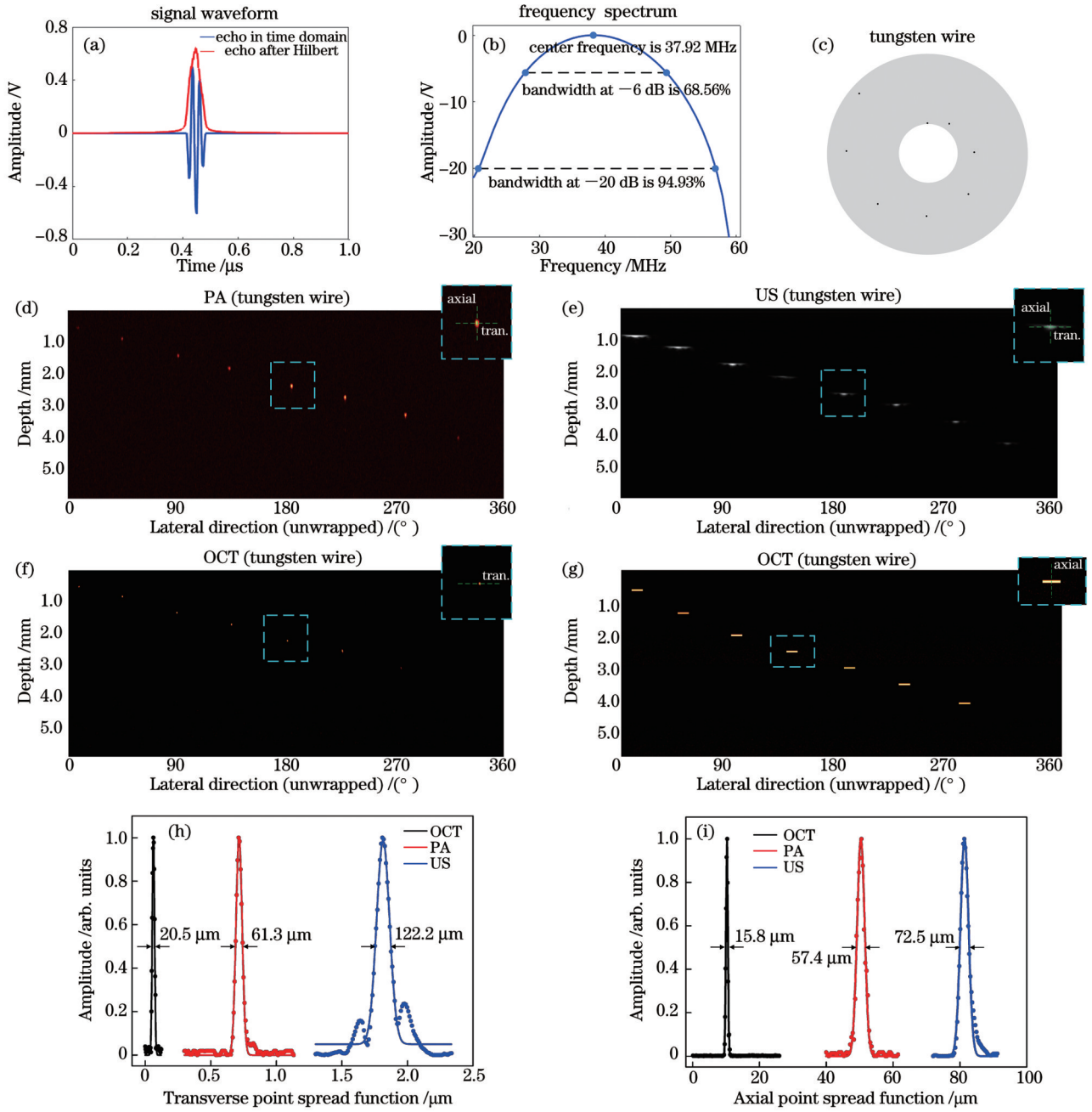

图 4　四模态成像系统性能测试。(a)超声回波信号；(b)超声换能器的频谱及带宽；(c)分辨率测试靶群示意图；(d)光声模态的横向和轴向分辨率成像结果；(e)超声模态的横向和轴向分辨率成像结果；(f)～(g)光学相干层析模态的横向和轴向分辨率结果；(h)三种模态的横向分辨率；(i)三种模态的轴向分辨率

Fig. 4　Performance testing of intravascular four-modality imaging system. (a) Ultrasonic echo signal; (b) spectrum and bandwidth of ultrasonic transducer; (c) schematic of resolution test target group; (d) lateral and axial resolution imaging results of PA modality; (e) lateral and axial resolution imaging results of US modality; (f)−(g) lateral and axial resolution imaging results of OCT modality; (h) lateral resolution test results of three imaging modalities; (i) axial resolution test results of three imaging modalities

该回波信号进行频谱分析得到超声换能器的主频参数，结果如图 4(b)所示。该超声换能器的探测主频为 37.92 MHz，−6 dB 带宽为 68.56%，−20 dB 带宽为 94.93%。进一步，为了测试该模态系统的成像分辨率，对螺旋排列的 8 根直径为 6 μm 的钨丝进行成像，钨丝排列方式如图 4(c)所示。图 4(d)～(g)是对上述样品的光声(PA)模态、超声(US)模态、光学相干层析(OCT)模态的重建图像，该成像结果由未作极坐标变换的 B-Scan 图像呈现。需要说明的是，光学相干层析模态的轴向分辨率需要通过对放置在不同位置处的平面镜(单层反射介质)进行成像来评估。选取焦点附近位置的成像结果作为系统的最佳成像分辨率进行评估，分辨率由选取位置处点扩散函数高斯拟合结果的半峰全宽(FWHM)决定。图 4(h)展示了三种模态的横向分辨率测试结果，光学相干层析、光声、超声模态的横向分辨率分别为 20.5、61.3、122.2 μm。图 4(i)展示了三种模态的纵向分辨率测试结果，光学相干层析、光声、超声模态的纵向分辨率分别为 15.8、57.4、72.5 μm。对于光声弹性(PAE)模态，其信号来自光声信号的上升沿，不包含深度信息，因而不存在轴向分辨率，并且其横向分辨率与光声模态的横向分辨率一致。

3.2　离体模拟样品实验

为了验证血管内多模态成像系统的成像性能，首先利用猪动脉血管、支架和脂质组成的模拟成像样品开展离体模拟样品的多模态成像实验。样品实物图如图 5(a)所示，图 5(b)展示了样品的剖面示意图。

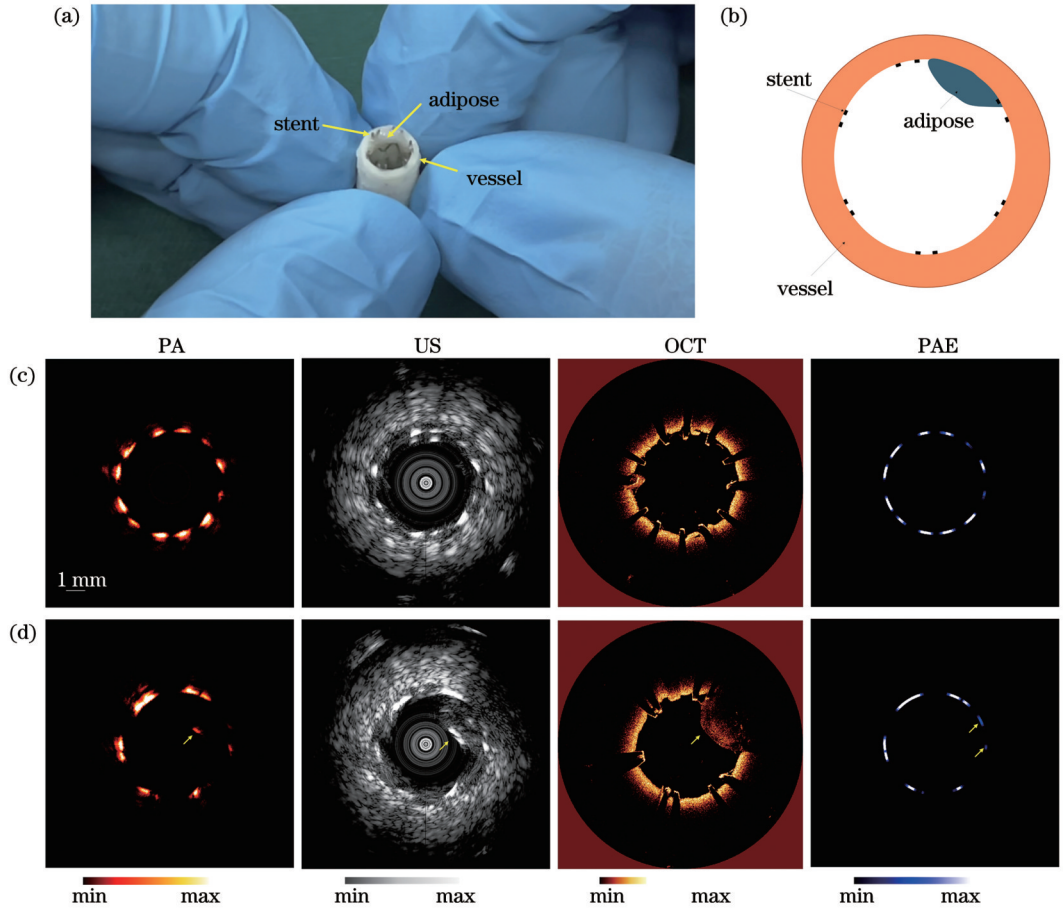

图 5　模拟样品的四模态成像结果。(a)血管-支架-脂质组合模拟样品照片；(b)模拟样品横截面示意图；(c)～(d)不同截面处的光声-超声-光学相干层析-光声弹性四模态成像结果

Fig. 5　Four-modality imaging results of simulated sample. (a) Photograph of vascellum-stent-lipid simulated sample; (b) schematic diagram of simulated sample cross-section; (c)–(d) PA-US-OCT-PAE imaging results of simulated sample at different sections

选取了两个不同位置处横截面的多模态成像结果进行展示。由图 5(c)所示的结果可以看出该截面没有脂质，只得到了支架和血管的四模态成像结果；由图 5(d)所示的结果可以看出该截面是有脂质部分的截面，得到了血管壁、支架和脂质的多模态成像结果。此外，支架从远端到近端，每个截面上钢丝的密度不同，选取的两个代表性横截面的光声、超声、光学相干层析以及光声弹性结果均显示了支架钢丝密度的变化。图 5(d)所示光声成像结果中的箭头所指位置为脂质存在的位置，在超声图像和光学相干层析图像中也能清晰地看到脂质分布；同时，有脂质分布位置与其他位置的光声弹性结果也具有明显差异。上述结果进一步表明了多模态成像系统对血管内斑块分布、组分以及机械弹性性质的成像能力，为后续对血管内斑

块的多方位多参数诊断提供了有力的影像技术支持。

3.3　兔腹主动脉在体实验

为了验证血管内多模态成像系统对活体成像的可行性，对高脂（97% 正常食物＋2% 猪油＋1% 胆固醇）喂养兔子（新西兰白兔，雄性，体重为 2.0～2.5 kg）的腹主动脉进行了在体实验。

实验前，使用动物麻醉剂对兔子进行麻醉，将兔子四肢固定在手术台上。首先，将兔子的一侧股动脉分离出来，在股动脉下方穿线并将远端结扎，近端穿线预留；然后，用镊子柄或止血钳撑起股动脉血管，用穿刺针穿刺血管，穿刺针进入血管后夹住股动脉，取出穿刺针头，并将导丝放入穿刺鞘管中经髂动脉进入腹主动脉，取出穿刺鞘管，置入一个 8 Fr 鞘管；最后，将一体化探头送入鞘管并且导丝进入腹主动脉，进行活体成像。探头的光声激发光最终输出的单脉冲能量为 1.6 μJ，对应 50 mJ/cm^2 的激光能量密度，远低于美国国家标准学会（ANSI）激光安全标准要求的 1 J/cm^2 的安全阈值[35]。每圈采集 500 个 A-line 信号，每个 A-line 采集 4096 个数据点，采集一圈时间为 200 ms。采集的数据由 GPU 进行实时图像重建，图像的帧速率为 5 frame/s。最终以 0.5 mm/s 的回撤速度获取了一段 20 mm 高脂喂养新西兰大白兔腹主动脉的四种模态图像。

三维成像结果如图 6（a）所示，成像结果在 0°～180°和 180°～360°分开展示。由光声和超声成像结果可以明显看出血管结构及血管内脂质的分布范围，而由光学相干层析成像结果可以看出整段血管的精

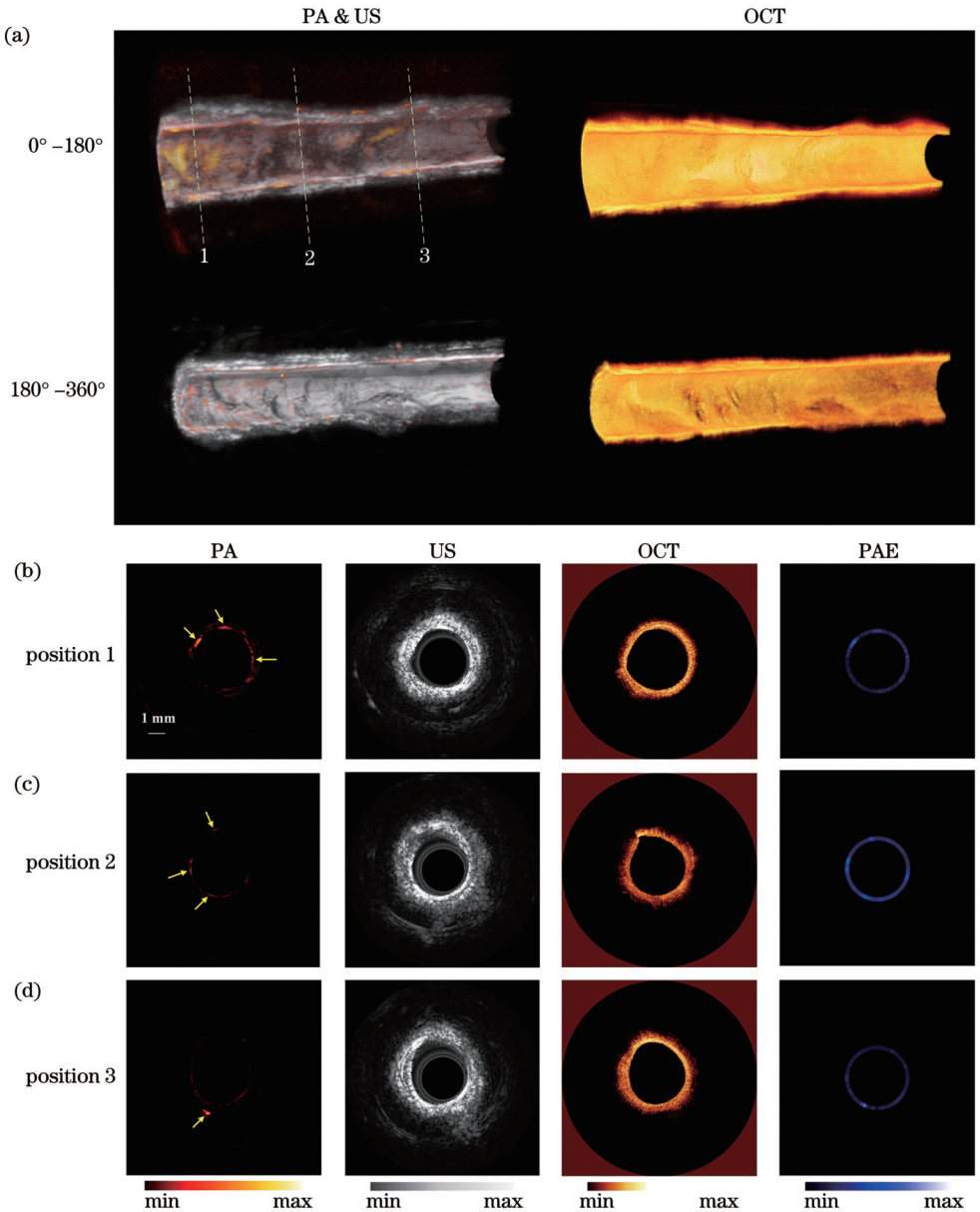

图 6　兔腹主动脉在体光声-超声-光学相干层析-光声弹性四模态成像结果。（a）三维成像结果；（b）～（d）腹主动脉三个不同位置的四模态成像结果

Fig. 6　*In vivo* PA-US-OCT-PAE four-modality imaging results of rabbit abdominal aorta. (a) Three dimensional imaging results; (b)–(d) four-modality imaging results at three different positions of rabbit abdominal aorta

细结构。如图 6(b)～(d)所示，选取三组具有代表性的图像对实验结果进行分析。从成像结果来看，具有光声信号的区域提示有脂质存在(如图中箭头所指处)。值得注意的是，系统的光声模态不仅能够对腹主动脉内壁的脂质成像[如图 6(b)和图 6(d)所示]，还能显示血管外膜附近的脂质[如图 6(e)所示]，从而证明了系统光声模态的深穿透能力。光声弹性模态的成像结果可以显示出存在脂质区域的弹性值。第一组成像结果的光声信号的幅值强于第二组的幅值，说明第一组成像结果所对应的血管截面处的脂质含量多于第二组。但第一组成像结果中截面的弹性值比第二组弹性值弱，说明随着脂质的积累，血管表面的弹性变小。在光学相干层析成像结果中可以清晰地识别整个血管的形态学结构。得益于超声成像的大穿透深度，超声图像能够清晰地显示出整个血管的轮廓。

总之，斑块兔模型的在体成像实验初步验证了本团队开发的四模态成像系统具有在体成像能力；同时，各个模态获取的信息能够相互补充，进而可以从 4 个维度对血管进行全面分析，为心血管相关疾病的诊断和治疗提供了一项新技术。

4 结　论

本团队开发了血管内光声-超声-光学相干层析-光声弹性多模态一体化成像探头及系统，并分别利用超声回波法和分辨率测试靶群对系统的超声探测主频和分辨率进行了测试。结果显示：系统的超声探测主频为 37.92 MHz；光学相干层析、光声、超声的横向分辨率分别为 20.5、61.3、122.2 μm，纵向分辨率分别为 15.8、57.4、72.5 μm。离体模拟样品和兔腹主动脉成像实验结果表明：该系统的光声模态可以提供高对比度的深度方向上脂质的分布；超声模态可以提供整个血管的结构信息；光学相干层析模态不仅可以评估支架的贴壁情况，还可以提供血管壁的精细结构；光声弹性模态可以提供斑块的弹性力学信息。血管内光声-超声-光学相干层析-光声弹性四模态系统无需更换导管或增加额外操作，只需通过单个一体化内窥探头的单次旋转扫描成像即可获得 4 个模态的图像，从而得到血管壁的精细结构、斑块内脂质的浓度、脂质在血管内壁的分布、斑块的弹性状态，对于临床医生全面理解评估动脉粥样硬化斑块的发生发展以及后续开展相应的诊疗具有重要意义。然而，受限于光声弹性的技术原理，在不产生光声信号的部位无法提取出光声弹性信号，导致了光声弹性图像的部分缺失。此外，本文仅基于光声弹性和光声成像对脂质进行了定性分析，有关定量实验如光声弹性灵敏度、光声成像探测脂类灵敏度的研究尚未开展；同时，本文仅对脂质斑块进行了动物模型的在体成像实验，缺乏其他类型斑块的实验数据，后续将开展其他斑块模型的动物实验。

血管内介入成像对精准评估斑块或其他血管内病变具有显著优势，在单一模态的血管内介入成像手段不能对病变进行精准诊断的情况下，多模态血管内介入成像能够从多方面对病变进行评估，从而帮助临床医生进行精准诊疗。因此，多模态血管介入成像将会是未来血管成像的重点发展方向之一。本团队设计的血管内四模态成像系统通过单一导管单次旋转回撤扫描成像即可得到多模态影像信息，并且这 4 种模态的信息相互补充，能够从结构、组分和力学特性等方面对血管内斑块进行全面评估。该系统有望为斑块易损性基础研究提供新手段，为血管内动脉粥样硬化斑块多模态信息监测提供更加全面的影像学信息，助力临床医生对动脉粥样硬化斑块的有效诊治。

参　考　文　献

[1] Libby P, Pasterkamp G, Crea F, et al. Reassessing the mechanisms of acute coronary syndromes: the "vulnerable plaque" and superficial erosion[J]. Circulation Research, 2019, 124(1): 150-160.

[2] Sanz J, Fayad Z A. Imaging of atherosclerotic cardiovascular disease[J]. Nature, 2008, 451(7181): 953-957.

[3] Shah P K. Mechanisms of plaque vulnerability and rupture[J]. Journal of the American College of Cardiology, 2003, 41(4): S15-S22.

[4] Virmani R, Burke A P, Farb A, et al. Pathology of the vulnerable plaque[J]. Journal of the American College of Cardiology, 2006, 47(8): C13-C18.

[5] Naghavi M, Libby P, Falk E, et al. From vulnerable plaque to vulnerable patient: a call for new definitions and risk assessment strategies: part I[J]. Circulation, 2003, 108(14): 1664-1672.

[6] Falk E, Shah P K, Fuster V. Coronary plaque disruption[J]. Circulation, 1995, 92(3): 657-671.

[7] De Korte C L, Sierevogel M J, Mastik F, et al. Identification of atherosclerotic plaque components with intravascular ultrasound elastography *in vivo*: a Yucatan pig study[J]. Circulation, 2002, 105(14): 1627-1630.

[8] Li Z H, Wang L, Hu X B, et al. Intravascular ultrasound elastography analysis of the elastic mechanical properties of atherosclerotic plaque[J]. The International Journal of Cardiovascular Imaging, 2017, 33(11): 1663-1671.

[9] Zhou Q, Chen Z. Multimodality imaging[M]. Heidelberg: Springer, 2020.

[10] Zhan K H, Wang L, Chen Z J, et al. Intravascular photoacoustic and autofluorescence imaging for detecting intraplaque hemorrhage: a feasibility study[J]. IEEE Journal of Selected Topics in Quantum Electronics, 2021, 27(4): 7100105.

[11] 李佳纹，陈忠平. 基于光学系统的血管内高集成多模态成像技术[J]. 中国激光, 2016, 43(12): 1200001.
Li J W, Chen Z P. Multimodality intravascular imaging technologies based on optical system[J]. Chinese Journal of Lasers, 2016, 43(12): 1200001.

[12] Garcia-Garcia H M, Costa M A, Serruys P W. Imaging of coronary atherosclerosis: intravascular ultrasound[J]. European Heart Journal, 2010, 31(20): 2456-2469.

[13] Kini A S, Vengrenyuk Y, Yoshimura T, et al. Fibrous cap thickness by optical coherence tomography *in vivo*[J]. Journal of the American College of Cardiology, 2017, 69(6): 644-657.

[14] 杨强, 祝连庆, 樊凡, 等. 正向切片光学相干断层成像系统的信号提取方法[J]. 光学学报, 2020, 40(7): 0711001.
Yang Q, Zhu L Q, Fan F, et al. Signal retrieval method of en-face optical coherence tomography system[J]. Acta Optica Sinica, 2020, 40(7): 0711001.
[15] Bouma B E, Villiger M, Otsuka K, et al. Intravascular optical coherence tomography[J]. Biomedical Optics Express, 2017, 8(5): 2660-2686.
[16] Zhang J, Yang S H, Ji X R, et al. Characterization of lipid-rich aortic plaques by intravascular photoacoustic tomography: *ex vivo* and *in vivo* validation in a rabbit atherosclerosis model with histologic correlation[J]. Journal of the American College of Cardiology, 2014, 64(4): 385-390.
[17] 李超, 孙明健, 马立勇, 等. 针对活体光声内窥成像的三维血管增强算法[J]. 中国激光, 2020, 47(9): 0907003.
Li C, Sun M J, Ma L Y, et al. Algorithm for three-dimensional enhancement of blood vessels in photoacoustic endoscopic *in vivo* imaging[J]. Chinese Journal of Lasers, 2020, 47(9): 0907003.
[18] 徐康, 王成, 张梦娇, 等. 动脉粥样硬化血管的光声频谱分析[J]. 激光与光电子学进展, 2021, 58(12): 1217001.
Xu K, Wang C, Zhang M J, et al. Photoacoustic spectrum analysis of atherosclerotic vessels[J]. Laser & Optoelectronics Progress, 2021, 58(12): 1217001.
[19] Ji X R, Xiong K D, Yang S H, et al. Intravascular confocal photoacoustic endoscope with dual-element ultrasonic transducer [J]. Optics Express, 2015, 23(7): 9130-9136.
[20] 陈重江, 杨思华, 邢达. 光声显微成像技术研究进展及其应用[J]. 中国激光, 2018, 45(3): 0307008.
Chen Z J, Yang S H, Xing D. Progress and application of photoacoustic microscopy technique[J]. Chinese Journal of Lasers, 2018, 45(3): 0307008.
[21] Wang Q, Shi Y J, Yang F, et al. Quantitative photoacoustic elasticity and viscosity imaging for cirrhosis detection[J]. Applied Physics Letters, 2018, 112(21): 211902.
[22] Wang P P, Chen Z J, Yang F, et al. Intravascular tri-modality system: combined ultrasound, photoacoustic, and elasticity imaging[J]. Applied Physics Letters, 2018, 113(25): 253701.
[23] Schaar J A, van der Steen A F W, Mastik F, et al. Intravascular palpography for vulnerable plaque assessment[J]. Journal of the American College of Cardiology, 2006, 47(8): C86-C91.
[24] Tian J W, Dauerman H, Toma C, et al. Prevalence and characteristics of TCFA and degree of coronary artery stenosis: an OCT, IVUS, and angiographic study[J]. Journal of the American College of Cardiology, 2014, 64(7): 672-680.
[25] Piao Z L, Ma T, Li J W, et al. High speed intravascular photoacoustic imaging with fast optical parametric oscillator laser at 1.7 μm[J]. Applied Physics Letters, 2015, 107(8): 083701.
[26] Wu M, Springeling G, Lovrak M, et al. Real-time volumetric lipid imaging *in vivo* by intravascular photoacoustics at 20 frames per second[J]. Biomedical Optics Express, 2017, 8(2): 943-953.
[27] Lei P, Wen X, Wang L, et al. Ultrafine intravascular photoacoustic endoscope with a 0.7 mm diameter probe[J]. Optics Letters, 2019, 44(22): 5406-5409.
[28] Li Y, Gong X J, Liu C B, et al. High-speed intravascular spectroscopic photoacoustic imaging at 1000 A-lines per second with a 0.9-mm diameter catheter[J]. Journal of Biomedical Optics, 2015, 20(6): 065006.
[29] Xie Z H, Shu C Y, Yang D Y, et al. *In vivo* intravascular photoacoustic imaging at a high speed of 100 frames per second[J]. Biomedical Optics Express, 2020, 11(11): 6721-6731.
[30] Lei P, Hao J H, Wang L, et al. Reliability assessment on intravascular photoacoustic imaging of lipid: *ex vivo* animal and human sample validation[J]. Journal of Biophotonics, 2020, 13 (12): e202000162.
[31] Mathews S J, Little C, Loder C D, et al. All-optical dual photoacoustic and optical coherence tomography intravascular probe [J]. Photoacoustics, 2018, 11: 65-70.
[32] Li X, Li J W, Jing J, et al. Integrated IVUS-OCT imaging for atherosclerotic plaque characterization[J]. IEEE Journal of Selected Topics in Quantum Electronics, 2014, 20(2): 196-203.
[33] Dai X J, Yang H, Shan T Q, et al. Miniature endoscope for multimodal imaging[J]. ACS Photonics, 2017, 4(1): 174-180.
[34] Leng J, Zhang J K, Li C G, et al. Multi-spectral intravascular photoacoustic/ultrasound/optical coherence tomography tri-modality system with a fully-integrated 0.9-mm full field-of-view catheter for plaque vulnerability imaging[J]. Biomedical Optics Express, 2021, 12(4): 1934-1946.
[35] Li J W, Thiele S, Quirk B C, et al. Ultrathin monolithic 3D printed optical coherence tomography endoscopy for preclinical and clinical use[J]. Light: Science & Applications, 2020, 9: 124.
[36] Munding C E, Chérin E, Alves N, et al. 30/80 MHz bidirectional dual-frequency IVUS feasibility evaluated *in vivo* and for stent imaging[J]. Ultrasound in Medicine & Biology, 2020, 46(8): 2104-2112.
[37] Wang J Q, Zheng Z, Chan J, et al. Capacitive micromachined ultrasound transducers for intravascular ultrasound imaging[J]. Microsystems & Nanoengineering, 2020, 6: 73.
[38] Dangi A, Agrawal S, Tiwari S, et al. Ring PMUT array based miniaturized photoacoustic endoscopy device[J]. Proceedings of SPIE, 2019, 10878: 1087811.
[39] Laser Institute of America. American national standard for safe use of lasers ANSI Z136. 1-2014[S]. Washington, D. C.: American National Standards Institute, 2013.

Intravascular Photoacoustic, Ultrasonic, Optical Coherence Tomography, and Photoacoustic Elastic Multimodal Imaging Method and System

Wan Yuyang[1,2], Lei Peng[3*], Xiong Kedi[1,2], Yang Sihua[1,2**]

[1]*MOE Key Laboratory of Laser Life Science & Institute of Laser Life Science, College of Biophotonics, South China Normal University, Guangzhou* 510631, *Guangdong, China*;

[2]*Guangdong Provincial Key Laboratory of Laser Life Science, College of Biophotonics, South China Normal University, Guangzhou* 510631, *Guangdong, China*;

[3]*Institute of Biological and Medical Engineering, Guangdong Academy of Sciences, Guangzhou* 510316, *Guangdong, China*

Abstract

Objective Rupture of vulnerable plaques with thrombosis is one of the major causes of most acute coronary syndromes. Plaque vulnerability is highly correlated with plaque structure, composition, and mechanical properties, which are typically characterized by

thin fibrous caps, lipid-rich necrotic cores, and severe stenosis; in addition, plaque vulnerability is also influenced by the mechanomechanical properties of the vessel wall and plaque. Intravascular photoacoustic (IVPA) imaging is an emerging intravascular imaging modality that can provide submillimeter resolution at penetration depths up to several centimeters and is capable of localizing and imaging lipids with high sensitivity and specificity. Simultaneously, plaque elastography can be performed through the IVPA signals without additional excitation; subsequently, the elastic mechanical properties of plaque can be evaluated. Although intravascular ultrasonography (IVUS) and intravascular optical coherence tomography (IVOCT) have been widely used in the clinical evaluation of plaque diagnosis, the current single intravascular imaging technology cannot assess the vulnerability of atherosclerotic plaques. For a comprehensive diagnosis, the clinicians need to obtain multiple features to fully identify and evaluate plaques. In this study, we proposed and developed an intravascular multimodal system that integrates four imaging modalities, namely, PA, US, OCT, and PAE. The information on plaque based on these four modalities can be obtained from a single probe via 360° rotation and synchronous retraction in one time, which is expected to provide a new interventional imaging method and tools for the understanding, diagnosis, and treatment of atherosclerotic plaques.

Methods The intravascular PA-US-OCT-PAE imaging system, which integrates the four subsystems of photoacoustic imaging, ultrasonic imaging, OCT, and photoacoustic elasticity, can be used to analyze the macroscopic and microscopic structural information of the blood vessel wall and to specifically identify the lipid components and to perform the elastic mechanics information diagnosis of lipid plaques. The software and hardware designs of each subimaging system and the timing control between the four modalities are shown in Fig. 1 and Fig. 2. The four-modality imaging results are obtained from the only imaging probe by a single-rotation scanning. The structural design of the integrated probe is shown in Fig. 1(b). As shown in the figure, the optical and acoustic paths are placed in parallel, and a miniature ultrasonic transducer with a main frequency of 30 MHz is used for PA signal reception and US signal excitation and reception. A single-mode fiber with an 8° angle end face is used to transmit PA excitation light and OCT detection light and receive the backscattered light of the OCT. A C-lens and coated mirror with a diameter of 0.5 mm are used to focus and deflect the beam so that the focal point of the light is located approximately 2 mm above the ultrasound transducer. The probe house is connected to the torsion coil for torque conduction. The imaging probe assembled with the above design scheme has only a rigid length of 3.6 mm and a diameter of 0.97 mm; this design improves the passability of the probe in tortuous blood vessels. *In vitro* experiments with simulated samples and *in vivo* imaging of rabbit abdominal aorta were conducted using the four-modality system with an integrated probe to demonstrate the feasibility of plaque analysis.

Results and Discussions The resolution of the PA-US-OCT-PAE imaging system was tested by using eight tungsten wires each with a diameter of 6 μm; the wires were arranged in a spiral form. As shown in Fig. 4, the lateral resolutions of OCT, PA, and US are 20.5, 61.3, and 122.2 μm, respectively. The axial resolutions of OCT, PA, and US are 15.8, 57.4, and 72.5 μm, respectively. The PAE signal, which is attributed to the rising edge of the PA signal, does not contain depth information. Hence, there is no axial resolution, and its lateral resolution is consistent with the PA modality. Further, *in vitro* experiments on simulated samples of porcine arterial vessels mixed with stents and lipid demonstrate the imaging capabilities of vascular structure identification, lipid detection, and elasticity measurement (Fig. 5). Finally, the *in vivo* experimental results of atherosclerosis model rabbits show clear vascular PA-US merged three-dimensional (3D) images, OCT 3D images, and PAE results of different sections (Fig. 6). The above results demonstrate the *in vivo* imaging capability of the intravascular four-modality system, thereby laying the foundation for its clinical translation. However, the system still has some limitations: the PAE signal cannot be extracted from the site where the PA signal is not generated, resulting in the partial absence of the elastic image; in addition, *in vivo* imaging experiments were only carried on animal models with lipid plaques, and trial data for other types of plaques are lacking.

Conclusions In this study, a intravascular multimodal PA-US-OCT-PAE imaging system with an integrated imaging probe were developed for the first time. The resolution of the multimodal system was tested by the ultrasonic echo method, and the excellent imaging capabilities of the system were demonstrated. The results of *in vitro* simulated samples and *in vivo* rabbit abdominal aorta imaging experiments showed that the PA modality can provide high-contrast images of the lipid distribution in the depth direction. The US modality can reveal the complete vascular structure. The OCT modality can not only evaluate the adherence of the stent but also provide the fine structure of the vessel wall. The PAE modality can provide the elastic mechanics information of the plaque. The information based on the four modalities, which is obtained by only one pullback imaging, is sufficient for comprehensively evaluating the structure, composition, and mechanical properties of the plaques. In conclusion, the intravascular multimodal imaging system is expected to provide a new and comprehensive method for research on plaque vulnerability and help clinicians to effectively diagnose and treat patients with atherosclerotic problems.

Key words medical optics; photoacoustic imaging; ultrasonic imaging; optical coherence tomography; photoacoustic elasticity imaging; intravascular multimodal imaging